

<https://doi.org/10.1038/s41529-025-00647-x>

# Influence of Mg and Al alloying additions on the corrosion mechanisms of Hot-dipped Zn-Mg-Al coatings: role of microstructure and phase distribution



A. D. Malla<sup>1</sup>✉, G. Williams<sup>1</sup>, D. A. Britton<sup>1</sup>, F. E. Goodwin<sup>2</sup>, Ana P. Domingos Cardoso<sup>3</sup>, T. Richards<sup>1</sup>, D. J. Penney<sup>1</sup> & J. H. Sullivan<sup>1</sup>

Systematic investigations into the individual effects of increasing alloying additions of Mg and Al on the corrosion mechanisms of Zn-Mg-Al coatings have demonstrated that microstructural phases and their surface distribution determine the anodic and cathodic behaviour of the coating. Increasing either Al and/or Mg from 1 to 3 wt.% improved the surface corrosion performance of the coating, with a greater effect observed for Al additions due to anodic deactivation. Mg additions led to cathodic deactivation due to a significant reduction in Zn dendrites at the surface. The corrosion rate was minimised by maximising the ternary eutectic area fraction at the coating surface. A 52% and 32% decrease in SVET-derived metal loss is achieved at 3 wt.% increase in Al and Mg, respectively.

Steel is among the most widely used materials across all major industrial sectors. The popularity of steel is due to its relatively low cost of production and processing, and most importantly, its exceptional mechanical properties. However, steel is susceptible to corrosion in various environments, reducing its service life unless costly maintenance is performed that increases cost, results in loss of use, and potentially increases safety risk. Coating steel with zinc (Zn) via hot-dip galvanising (HDG) is an effective way to increase its corrosion resistance<sup>1,2</sup>. Alloying Zn with Aluminium (Al) and Magnesium (Mg) together has proven to have further enhanced the corrosion resistance of Zn<sup>3–5</sup>, especially in the presence of chloride ions<sup>6–10</sup>. Zn-Al coatings are predominantly used in the building industry, whereas Zn-Mg-Al (ZMA) coatings are being adopted for white goods, for solar cell frames, and in the automotive industry because of their superior corrosion properties and mechanical properties such as excellent scratch resistance, microhardness and galling behaviour<sup>11</sup>. Zn-11Al-3Mg-0.2Si, Zn-6Al-3Mg and Zn- (1–2 wt. %) Al- (1–2 wt. %) Mg are some of the commercially available ZMA coatings<sup>10,12</sup>. Because of manufacturers' existing patents, each producer tends to develop their own bespoke alloy composition and register it with their product name. Therefore, in Europe, Al content varies from 1 – 3.7 wt. % and Mg varies from 1 – 3 wt. %. Further quaternary alloying additions such as Germanium (Ge), Calcium (Ca), Titanium (Ti), and Silicon (Si) addition to Zn-Mg-Al have also been investigated<sup>13,14</sup>.

The addition of Al and Mg to Zn results in the formation of a complex microstructure containing Zn phases, Al phases and intermetallics (IMs)

such as MgZn<sub>2</sub> and Mg<sub>2</sub>Zn<sub>11</sub>. The Al phases are more noble (more electropositive) compared to the Zn phases<sup>12,15,16</sup>. In contrast, the IMs, MgZn<sub>2</sub>, and Mg<sub>2</sub>Zn<sub>11</sub> undergo preferential anodic dissolution, galvanically protecting the Zn surfaces<sup>17–19</sup>. Mg<sup>2+</sup> ions released react with hydroxyl ions to form magnesium hydroxide (Mg(OH)<sub>2</sub>), a cathodic oxygen reduction reaction suppressor<sup>15,20</sup>. In addition, the Mg(OH)<sub>2</sub> buffers the local pH to alkaline values (~pH 10.2)<sup>21</sup> at which the Zn surfaces and corrosion products such as simonkolleite are stable<sup>6,14,22</sup>. At alkaline pH, the aluminium phases become anodically active to produce aluminates, which react with Mg<sup>2+</sup> to form insulating double-layered hydroxides (LDH)<sup>19</sup>.

The chemical composition of ZMA coatings and their production parameters<sup>23</sup> determines their microstructure. For example, Zn - 2 wt. % Al - 2 wt. % Mg is composed of primary Zn dendrites, binary eutectic and ternary eutectic<sup>19,24</sup>, whereas Zn - 3 wt. % Al - 3 wt. % Mg exhibited no primary Zn<sup>25</sup>. Investigations have also revealed that the modification of the ZMA microstructure significantly changes the corrosion resistance and corrosion mechanism<sup>8,23,26</sup>. In recent times, a number of investigations have been conducted on the influence of the separate effects of Al<sup>27,28</sup> or Mg<sup>11,29–31</sup> content on the corrosion resistance of ZMA, but limited investigations have been conducted on combined Al and Mg content<sup>32</sup>. Investigations so far have reported enhancement of corrosion resistance due to an increase in both Al and Mg<sup>11,27–31</sup>. However, a mechanistic investigation on the change in corrosion mechanism due to the systematic variation in Al and/or Mg content is absent. Therefore, developing a fundamental understanding of

<sup>1</sup>Corrosion and Coatings Group, Department of Materials, Swansea University, Bay Campus, Fabian Way, Crymlyn Burrow, Swansea, UK. <sup>2</sup>International Zinc Association, Durham, NC, USA. <sup>3</sup>International Zinc Association, Brussels, Belgium. ✉e-mail: [amar.malla@swansea.ac.uk](mailto:amar.malla@swansea.ac.uk)

each element's effects in the ternary systems would thus help to make informed decisions regarding the compositional design of coatings for new products and markets.

In this investigation, a hot-dip process simulator (HDPS) was used to produce ZMA coatings with systematic changes in Al and Mg levels in the range of 1–3 wt.% to assess the individual elemental contributions in changes to microstructure and corrosion mechanisms. This paper aims to elucidate the individual effects of Mg and Al on the anodic and cathodic activation or deactivation pathways of Zn-Mg-Al (ZMA) coatings.

## Results

### Materials characterisation

The targeted and ICP-OES measured alloy compositions are presented in Table 1. The targeted and measured alloy compositions in wt.% demonstrated some variance in measured compositions for Zn-1Mg-1Al, Zn-1Mg-3Al and Zn-3Mg-1Al, but the samples displayed systematic changes in alloying elemental additions, enabling their individual effects to be assessed. The variation in the targeted and measured compositions could possibly have occurred due to various factors, such as losses due to dross and oxidation. Furthermore, errors can occur due to weight changes as samples are

being made, and precise measurements are difficult to make due to the dynamic conditions of the pot.

Figure 1 shows the representative SEM images of both the cross-section and surface of the Zn-1Mg-1Al, Zn-1Mg-3Al, Zn-3Mg-1Al and Zn-3Mg-3Al coatings. The base Zn-1Mg-1Al coating (Fig. 1a, b) was composed of three different phases; primary zinc dendrites, binary eutectic and ternary eutectic. Large primary Zn dendrites were surrounded predominantly by a lamellar binary eutectic ( $\text{MgZn}_2$  and Zn) with Al mainly contained in discrete Al-rich nodules in the ternary eutectic. The SEM image of cross-section (Fig. 1a) shows that primary Zn dendrites often transversed the entire coating thickness from the steel substrate to the surface and through-coating eutectic pathways were also present between the Zn dendrites.

Increasing the Al content from 1 wt.% to 3 wt.%, i.e., (Zn-1Mg-3Al), has resulted in distinct changes in the microstructure (Fig. 1 c-d)). The microstructure was composed of large primary Zn dendrites with numerous small Al-rich phases (dark) co-located at the peripheries of the primary Zn dendrites. These phases were surrounded by a matrix of ternary eutectic (Zn,  $\text{MgZn}_2$  and Al nodules). Binary eutectic was absent in all observed regions of the coating. The SEM image of the cross-section (Fig. 1(c)) demonstrated that the primary Zn dendrites were generally smaller and more numerous than the base Zn-1Mg-1Al.

Increasing the Mg content from 1 wt.% to 3 wt.%, i.e., (Zn-3Mg-1Al), has resulted in significant changes in the microstructure (Fig. 1e, f). The microstructure was composed of primary Zn dendrites surrounded by large areas of binary eutectic. Small areas of ternary eutectic were also observed with Al-rich regions sometimes present within this phase. The SEM image of the cross-section (Fig. 1e) revealed that the primary Zn dendrites were generally smaller than the two previous coatings with a reduction in the number of dendrites reaching the coating surface and having nucleated at the steel/coating interface. In addition, the surface of the sample was rich in eutectic compared with the base Zn-1Mg-1Al and Zn-1Mg-3Al.

**Table 1 | ZMA coatings targeted chemical composition**

Sample	Targeted Mg (wt.%)	Measured Mg (wt.%)	Targeted Al (wt.%)	Measured Al (wt.%)	Zn
Zn-1Mg-1Al	1	1.3	1	1.2	Bal
Zn-1Mg-3Al	1	1	3	4	Bal
Zn-3Mg-1Al	3	3.6	1	1.2	Bal
Zn-3Mg-3Al	3	2.9	3	2.9	Bal

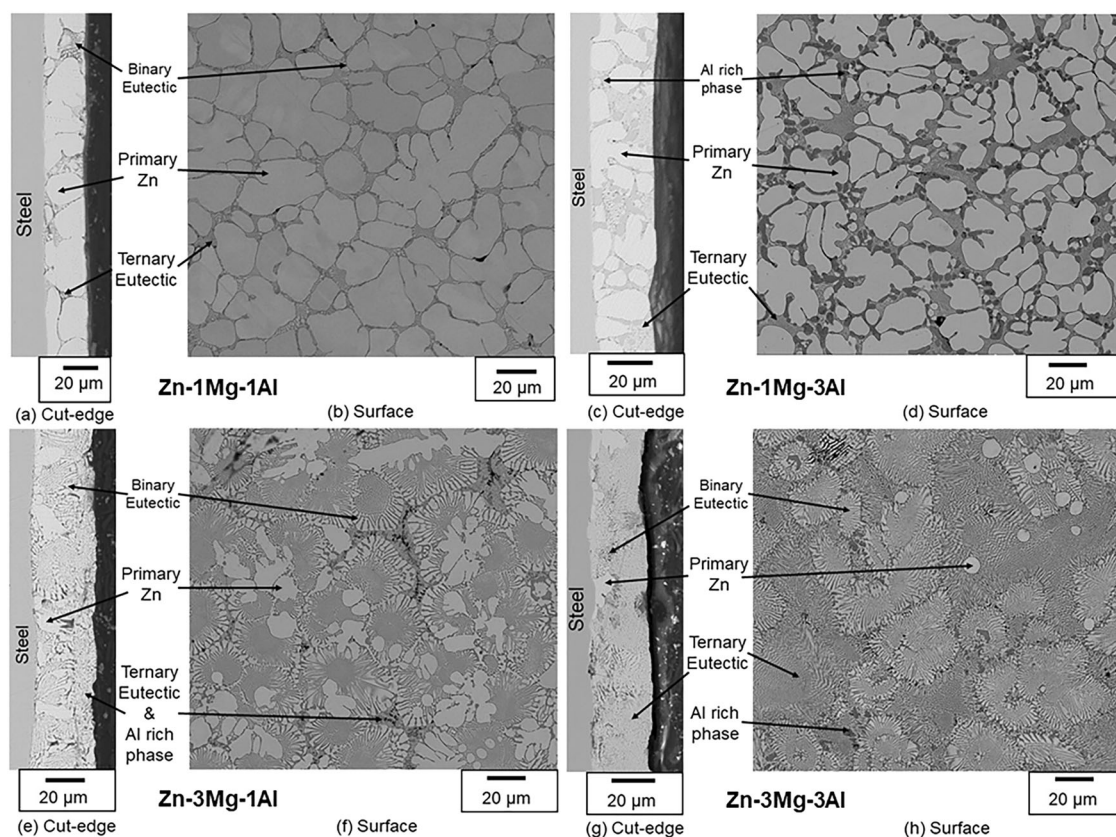


**Fig. 1 | SEM images showing the cross-section and surface microstructures of Zn-Mg-Al. a, c, e, g** Shows cut-edge microstructure and **b, d, f, h** shows the surface microstructure. The variation in Mg and Al content has led to significant changes within the microstructure of Zn-Mg-Al coatings.

**Fig. 2 | EDS elemental colour maps of Zn-Mg-Al.** The results are for (a) Zn-1Mg-1Al (b) Zn-1Mg-3Al (c) Zn-3Mg-1Al and d Zn-3Mg-3Al. The images show the distribution of Zn, Mg and Al within the microstructure of Zn-Mg-Al coatings.

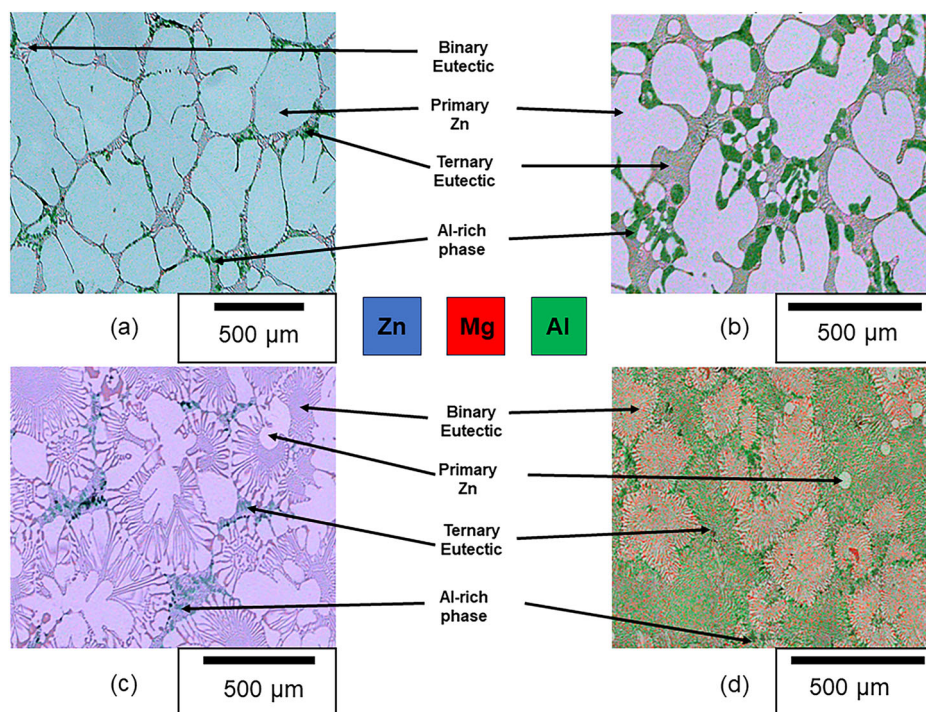


**Table 2 | Composition of phases present within ZMA samples obtained using EDS**

Zn-1Mg-1Al			
	Zn (wt.%)	Mg (wt.%)	Al (wt.%)
Primary Zn	99.06 ± 0.12	0.28 ± 0.05	0.65 ± 0.08
Binary Eutectic	94.62 ± 1.90	3.90 ± 2.17	1.49 ± 0.28
Ternary Eutectic	93.87 ± 1.25	4.57 ± 1.57	1.57 ± 0.31
Zn-1Mg-3Al			
Primary Zn	97.86 ± 0.11	0.29 ± 0.08	1.85 ± 0.10
Ternary Eutectic	88.34 ± 0.78	3.62 ± 0.38	8.04 ± 0.43
Al-rich Phase	72.58 ± 0.37	0.77 ± 0.33	26.65 ± 0.58
Zn-3Mg-1Al			
Primary Zn	99.07 ± 0.09	0.40 ± 0.08	0.52 ± 0.03
Binary Eutectic	94.89 ± 0.65	3.87 ± 0.30	0.98 ± 0.07
Ternary Eutectic	91.66 ± 3.07	2.64 ± 0.75	5.71 ± 2.92
Zn-3Mg-3Al			
Primary Zn	98.49 ± 0.17	0.44 ± 0.08	1.07 ± 0.11
Binary Eutectic	94.55 ± 0.11	4.25 ± 0.14	1.19 ± 0.08
Ternary Eutectic	89.29 ± 0.88	3.73 ± 0.50	6.98 ± 1.12

Increasing both Al & Mg content from 1 wt.% to 3 wt.%, i.e. (Zn-3Mg-3Al), has resulted in complete changes in the microstructure (Fig. 1g, h). The microstructure was composed almost entirely of eutectic with regions of both binary eutectic and ternary eutectic. Small quantities of primary Zn dendrites and discrete Al-rich regions were also observed. The SEM image of the cross-section (Fig. 4(g)) revealed that the primary Zn dendrites were small, nucleating from the steel substrate with eutectic regions dominating the volume fraction of the coating. The surface of the sample appeared to be rich in eutectic compared with the other three samples Zn-1Mg-1Al, Zn-1Mg-3Al and Zn-3Mg-1Al.

### Microstructural comparisons across all samples

Energy dispersive X-ray spectroscopy (EDS) was employed to identify the distribution of elements within the experimental samples. Elemental maps identifying the elements Zn, Mg and Al were produced using Oxford Instruments SEM/EDS software and are shown in Fig. 2. The elemental composition of each phase, calculated from 3 different areas of each type of phase, is presented in Table 2.

XRD was further performed to investigate different phases present within the coatings' microstructures, and the results obtained are presented in Fig. 3. The XRD patterns indicate that all coatings contained Zn and Al solid solution phases, whereas Mg was present as three different Zn intermetallic phases:  $\text{MgZn}_2$ ,  $\text{Mg}_2\text{Zn}_{11}$ , and  $\text{Mg}_3\text{Zn}_{13}$ . Increasing the Mg to 3 wt. % tends to increase the intensity and number of peaks corresponding to  $\text{MgZn}_2$  and  $\text{Mg}_2\text{Zn}_{11}$ , showing more intermetallic formation. Whereas, increasing the Al to 3 wt. % increases the number of Al peaks, showing more Al-rich phases. This was observed for both Zn-1Mg-3Al and Zn-3Mg-3Al.

This increase in the formation of intermetallic and Al-rich phases could potentially alter the phase composition. Hence, further microstructural analysis (volume fraction measurement) was conducted and is presented in Table 3. The volume fractions of primary Zn and eutectic (binary + ternary eutectic combined) were calculated for five cross-section images (250 µm in length) of each coating. The table represents the relative effects of Mg and Al on the measured volume fractions. The base coating Zn-1Mg-1Al had a through coating volume fraction of 77.75% primary Zn and 22% eutectic phase. When either Al or Mg levels were increased to 3 wt.%, an increase in the eutectic phase was observed. However, the increase in the eutectic phase was significantly greater for 3 wt.% Mg additions with 68% eutectic volume fraction compared to 37% when Al was increased to 3 wt.%. In addition, when both Mg and Al were increased to 3 wt.% the microstructure became almost wholly eutectic with eutectic volume fraction of 94.01% (Table 3).

### Study of the electrochemical behaviour of ZMA coatings

The surface corrosion was investigated for the ZMA coatings using a combination of in-situ imaging and electrochemical techniques. All the corrosion experiments were performed in 0.17 mol.L<sup>-1</sup> NaCl pH 7 solution. 0.17 mol.L<sup>-1</sup> NaCl pH 7 was used as our previous investigations on Zn and



**Fig. 3 | XRD patterns obtained for Zn-Mg-Al coatings.** The XRD pattern shows the presence of intermetallic  $\text{MgZn}_2$ ,  $\text{Mg}_4\text{Zn}_7$  and  $\text{Mg}_2\text{Zn}_{11}$  in all four coatings.

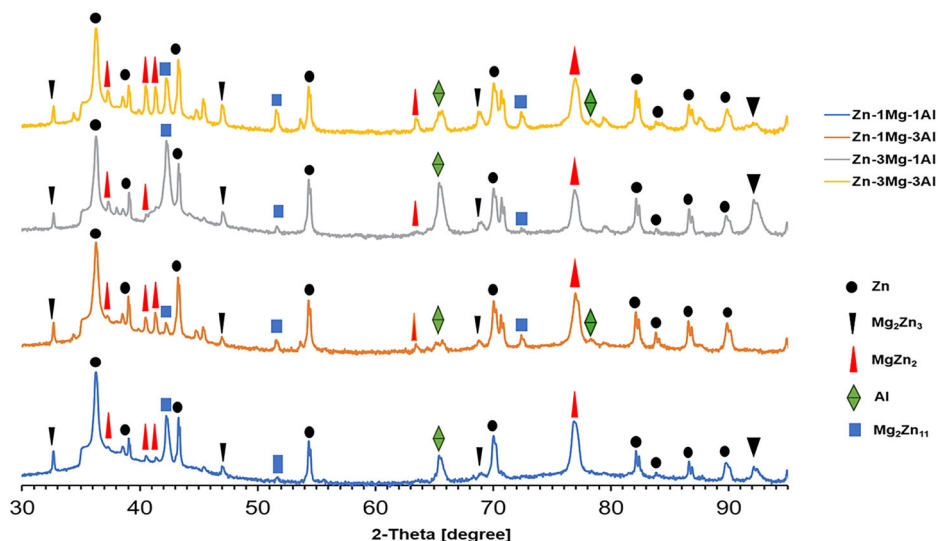


**Table 3 | Volume fraction of phase present in ZMA samples**

Sample	Primary Zn (%)	Eutectic (%)
Zn-1Mg-1Al	77.75 ± 1.56	22.25 ± 1.56
Zn-1Mg-3Al	63.42 ± 4.96	36.58 ± 4.96
Zn-3Mg-1Al	31.69 ± 12.02	68.31 ± 12.01
Zn-3Mg-3Al	5.99 ± 1.49	94.01 ± 1.49

Zn-based alloys/coatings were conducted in 0.17 M NaCl. Therefore, it has been used for consistency and to compare different alloys/coatings.

### Investigation of corrosion mechanisms using time-lapse microscopy (TLM)

**Zn-1Mg-1Al.** The corrosion mechanism occurring at the microstructural level was studied using TLM. Figure 4 and Video 1 (V1) show the corrosion behaviour of the base Zn-1Mg-1Al coating over 24 h in 0.17 mol.L<sup>-1</sup> NaCl pH 7 solution. Anodic features (presenting as a dark region) developed from the onset of the exposed area (see Video 1) and after ~2 h a large anodic feature (metal oxidation/dissolution) was established in the upper left quadrant of the exposed circular area (Fig. 4b). Figure 5 presents a cropped region showing the initiation and progression of an anode over the first 100 min of exposure. The anodic regions were identified based on image contrast and the movement of the anodic front. The anodic initiation occurred by minute 50 in the interdendritic eutectic phase and preferentially progressed via the eutectic, often leaving intact “islands” of primary Zn. Similar phenomena were previously observed on ZMAs using this technique<sup>14,17,23</sup>. A corrosion product is formed at some distance from the anode. Corrosion products are formed when the counter-current of metal cations from the anode and hydroxide anions from the cathode react with each other. Corrosion product precipitation occurred on the sample surface once the solubility limit of the corrosion product in the solution was locally exceeded<sup>14,17</sup>. Further anodes initiated over time and always initiated and progressed preferentially through the eutectic phase. However, Zn dendrites were consumed when the local eutectic regions had corroded.

**Zn-1Mg-3Al.** Figure 6 and Video 2 (V2) show the corrosion behaviour of the Zn-1Mg-3Al coating over 24 h in 0.17 mol.L<sup>-1</sup> NaCl pH 7 solution. Figure 7I presents a cropped region showing the initiation and progression of the anode during the first 100 min of exposure. For this coating, the corrosion mechanism was rather different compared to the base Zn-1Mg-1Al. From Fig. 6 and V2, it was somewhat difficult to

ascertain in which phase initiation of the anode occurred due to image resolution and microstructural complexity. However, once the anode had initiated, the primary Zn dendrites were then routinely attacked along with the eutectic without the sole preferential attack of the eutectic observed for the base Zn-1Mg-1Al. Through consideration of the cropped region in Fig. 7I, it could be seen that anode initiation had begun within the eutectic phase by minute 25 (Fig. 7Ib, with subsequent progression through both the eutectic and Zn dendrites over the next 75 min. Additionally, the Al-rich phases appeared relatively uncorroded after 100 minutes and in fact remained uncorroded after 24 h, as shown in Fig. 7(II).

**Zn-3Mg-1Al.** Figure 8 and Video 3 (V3) show the corrosion behaviour of the Zn-3Mg-1Al coating over 24 h in 0.17 mol.L<sup>-1</sup> NaCl pH 7 solution. Figure 9 presents a cropped region showing the initiation and progression of the anode during the first 100 minutes of exposure. From Fig. 8 and V3, it can be seen that corrosion initiated and progressed preferentially through the binary eutectic regions that were the dominant phase in the microstructure of the exposed surface. Figure 8 also showed that the number of anodic features initiated over the course of the 24 h experiment was greater for this coating, suggesting that this system experienced numerous activations and deactivations of anodic events rather than progressive attack across the surface from a limited number of sites. This experiment also showed precipitation and re-solubilisation of the corrosion product as anodic features initiated and progressed across the microstructure.

**Zn-3Mg-3Al.** Figure 10 and Video 4 (V4) show the corrosion behaviour of the Zn-3Mg-3Al coating over 24 h in 0.17 mol.L<sup>-1</sup> NaCl pH 7 solution. Figure 11 presents a cropped region showing the initiation and progression of the anode during the first 100 mins of exposure. The microstructure of Zn-3Mg-3Al was predominantly a mixture of binary and ternary eutectic (Fig. 1g, h and Fig. 10A). Similarly to Zn-3Mg-1Al and base Zn-1Mg-1Al, the corrosion initiated and spread preferentially through the binary eutectic present at the exposed surface. The anode subsequently progressed into the ternary eutectic as shown in Fig. 11 although progression slowed somewhat for this particular feature once the ternary eutectic became attacked.

To better understand the corrosion behaviour of the different coatings, it is critical to understand the area fraction of phases within the microstructure at the actual surface exposed to the electrolyte. Therefore, the TLM image taken at 100X magnification of a 0.78 mm<sup>2</sup> area of all four coatings exposed to electrolyte was analysed. These area fractions of primary Zn and

**Fig. 4 | Time-lapse Microscopy images of Zn-1Mg-1Al taken under immersion conditions in 0.17 mol.L<sup>-1</sup> NaCl pH 7 solution.** The images shown were taken at **a** 2 min **b** 8 h **c** 16 h and **d** 24 h.

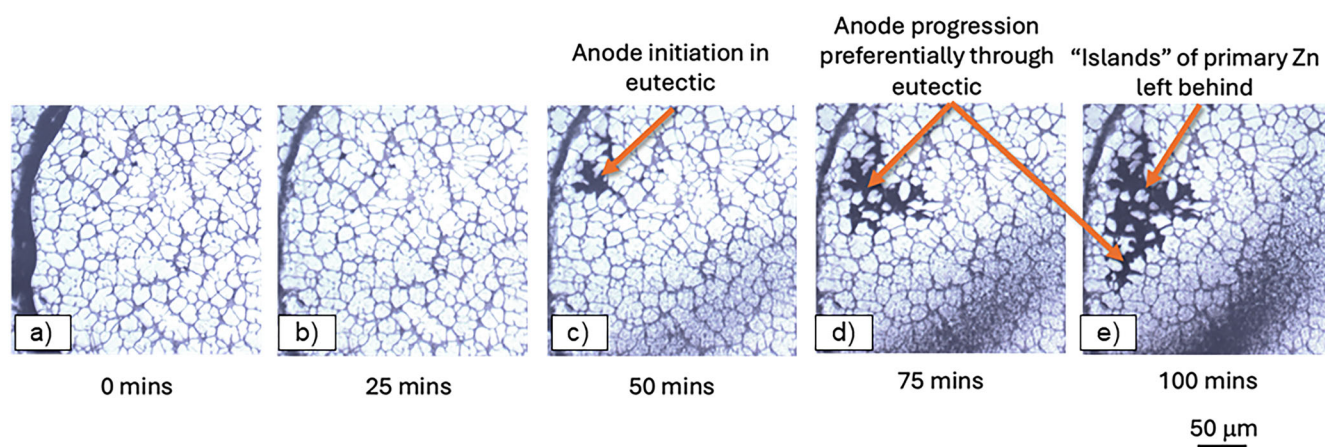
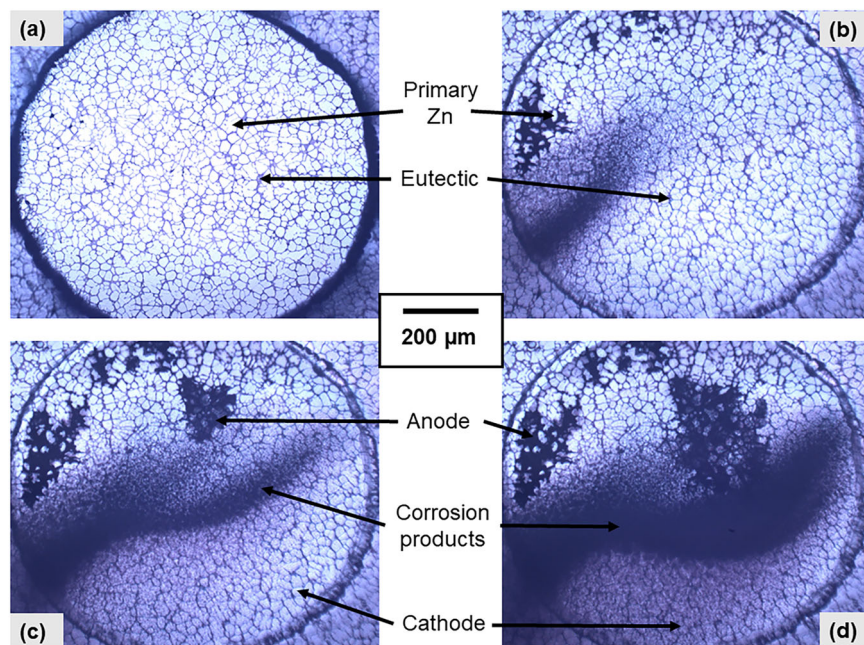


**Fig. 5 | Time-lapse Microscopy images of Zn-1Mg-1Al taken under immersion conditions in 0.17 mol.L<sup>-1</sup> NaCl pH 7 solution.** The images shown were taken at **a** 0 min **b** 25 min **c** 50 min **d** 75 min and **e** 100 min. The images show the initiation and progression of an anode over the first 100 min of exposure.

eutectic phase at the surfaces of ZMA coatings exposed to the electrolyte during the TLM experiments are presented in Table 4.

From Table 4, it was observed that increasing either the Al or the Mg levels individually to 3 wt.% had a significant effect on the surface area phase fraction compared to the base Zn-1Mg-1Al. Mg had a greater effect with an increase in the eutectic area fraction from 42.41 to 88.81% compared with an increase from 42.41 to 76.22% for Al. Furthermore, when both Mg and Al levels were increased to 3 wt.% the surface was almost wholly eutectic.

### Electrochemical measurements

Two types of electrochemical experiments, open circuit potential (OCP) and linear polarisation resistance (LPR), were performed to further investigate the influence of Mg and Al content ( $\leq 3$  wt.%) on ZMA coatings. The experiments were initiated immediately after the introduction of the electrolyte. All the electrochemical data presented are the mean values of three experiments.

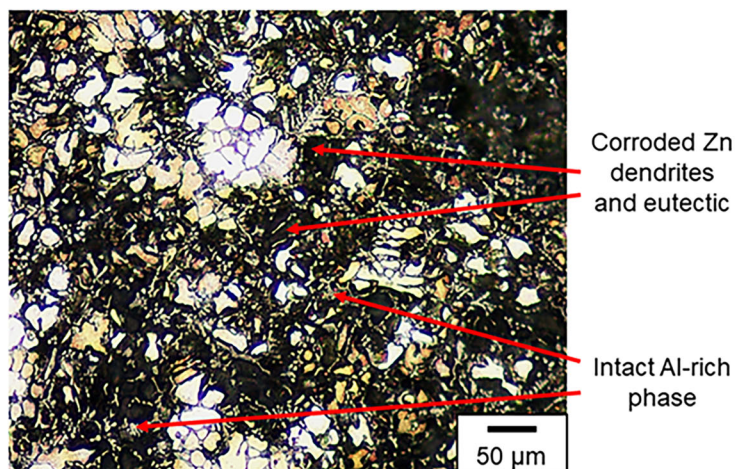
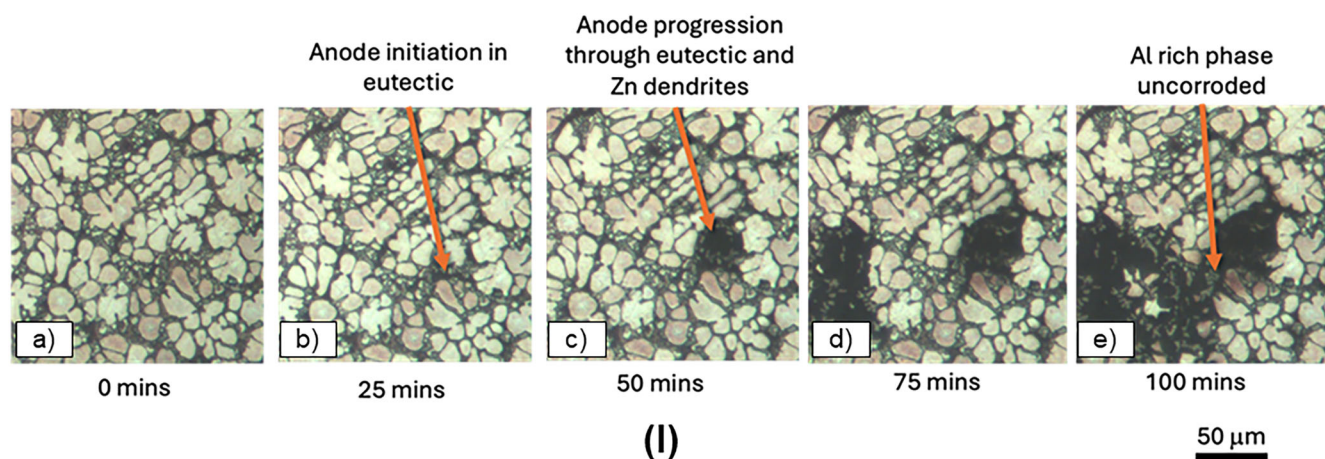
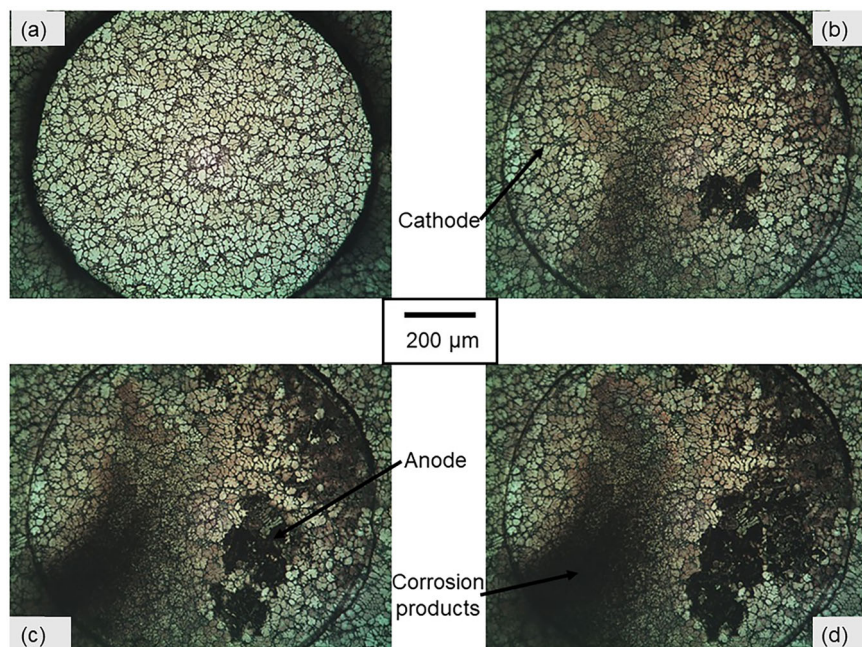
### Open circuit potential

Figure 12 shows the average OCP measurements of four ZMA coatings immersed in 0.17 mol.L<sup>-1</sup> NaCl pH 7, over 24 h. With respect to the base Zn-1Mg-1Al coating, Al additions resulted in an overall increase in OCP, whereas Mg additions led to a significant drop in OCP. For the Zn-3Mg-3Al, the OCP was more negative than the base Zn-1Mg-1Al, demonstrating the dominant effects of the increased Mg levels compared to Al. However, the OCP was not as negative as for the Zn-3Mg-1Al, thus demonstrating the competing effects of the Mg and Al additions.

The complete set of three repeat experiments for each coating was statistically summarised and is presented in the box plot in Fig. 13. This figure highlights the competing effects of the Mg and the Al additions with regard to decreasing and increasing the OCP of the coating, respectively, in comparison to the base Zn-1Mg-1Al. The high potential outlying points for each coating reflect the initial potential of the coating due to the presence of an air-formed oxide. Upon immersion, this oxide breaks down and the potential decreases to that of the oxide-free coating surface.



**Fig. 6 | Time-lapse Microscopy images of Zn-1Mg-3Al taken under immersion conditions in 0.17 mol.L<sup>-1</sup> NaCl pH 7 solution. The images shown were taken at a 2 min b 8 h c 16 h and d 24 h.**



**Fig. 7 | Time-lapse Microscopy images of Zn-1Mg-3Al taken under immersion conditions in 0.17 mol.L<sup>-1</sup> NaCl pH 7 solution. (I) The images taken at (a) 0 min (b) 25 min (c) 50 min (d) 75 min and (e) 100 min show the initiation and progression of an**

**anode over the first 100 minutes of exposure. (II) The image demonstrates corrosion of the primary Zn dendrites and the eutectic whilst the Al-rich dendritic phase remained generally intact after 24 h immersion in 0.17 mol.L<sup>-1</sup> NaCl pH 7 solution.**



**Fig. 8 | Time-lapse Microscopy images of Zn-3Mg-1Al taken under immersion conditions in 1 wt.% NaCl pH 7 solution.** The images shown were taken at a 2 min b 8 h c 16 h and d 24 h.

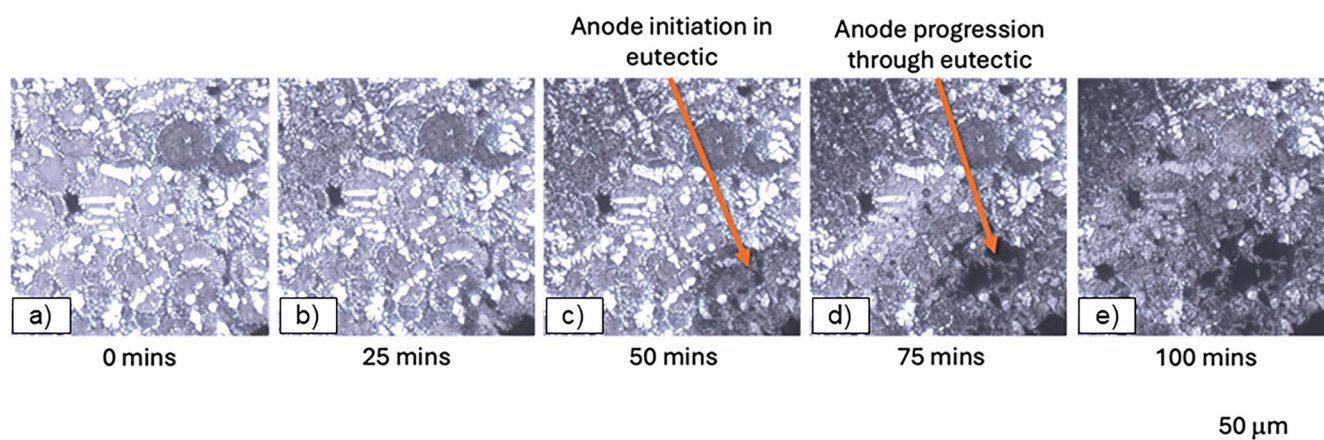
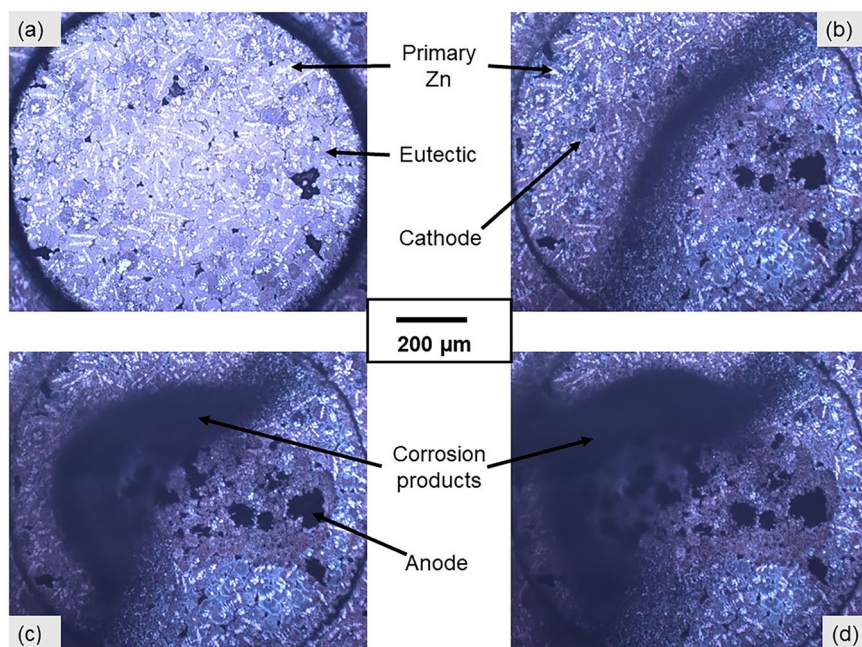


**Fig. 9 | Time-lapse Microscopy images of Zn-3Mg-1Al taken under immersion conditions in 0.17 mol.L<sup>-1</sup> NaCl pH 7 solution.** The images taken at (a) 0 min (b) 25 min (c) 50 min (d) 75 min and e 100 min show the initiation and progression of an anode over the first 100 min of exposure.

### Linear polarisation resistance (LPR)

Figure 14 shows the average LPR measurements of four ZMA coatings immersed in 0.17 mol.L<sup>-1</sup> NaCl pH 7 over a 24 h time period. In LPR experiments, higher resistance ( $R_p$ ) is representative of a lower corrosion current ( $i_{corr}$ ). The Zn-1Mg-3Al demonstrated the largest increase in  $R_p$  values compared to base Zn-1Mg-1Al, hence, a reduction in corrosion kinetics. The Zn-3Mg-1Al was kinetically somewhat similar to the base Zn-1Mg-1Al however, Zn-3Mg-3Al displayed a general reduction in corrosion kinetics.

Figure 15 shows box plots of all the average LPR data and provides further insight into the effect of the Mg and Al additions on the corrosion kinetics. The box plots demonstrated that the Zn-1Mg-3Al not only increased the median of corrosion resistance with respect to the base coating, Zn-1Mg-1Mg, but also provided the highest maximum resistance and hence the lowest corrosion rate of the coatings investigated in this study. The Zn-3Mg-1Al and Zn-3Mg-3Al coatings both displayed higher median values than the Zn-1Mg-1Al and a lower spread of data overall, implying that the systems had lower and more predictable corrosion kinetics.

### Investigation of corrosion behaviour using the scanning vibrating electrode technique (SVET)

The SVET was utilised to further explore the kinetic corrosion behaviour and corrosion performance of ZMA coatings in 0.17 mol.L<sup>-1</sup> NaCl pH 7 solution over 24 h. The data presented are the average values of three SVET experiments. The data captured from the hourly SVET scans were used to calculate a semi-quantitative metal loss for each scan and summed to provide a cumulative 24 h metal loss. The time-dependent average kinetic SVET metal loss is presented in Fig. 16 and the average total metal losses over 24 h are presented in Table 5. Figure 16 showed that the base Zn-1Mg-1Al demonstrated the highest average metal loss per hour and thus, the highest cumulative average metal loss of 11.48 g.m<sup>-2</sup> as shown in Table 5. The alloying additions all provided improved corrosion performance with the subsequent order of performance from the highest to lowest corrosion rate being:

$$\text{Zn} - 1\text{Mg} - 1\text{Al} (11.24\text{g.m}^{-2}) > \text{Zn} - 3\text{Mg} - 1\text{Al} (7.54\text{g.m}^{-2}) \\ > \text{Zn} - 3\text{Mg} - 3\text{Al} (6.49\text{g.m}^{-2}) > \text{Zn} - 1\text{Mg} - 3\text{Al} (5.31\text{g.m}^{-2})$$

**Fig. 10 | Time-lapse Microscopy images of Zn-3Mg-3Al taken under immersion conditions in 0.17 mol.L<sup>-1</sup> NaCl pH 7 solution. The images shown were taken at a 2 min b 8 h c 16 h and d 24 h.**

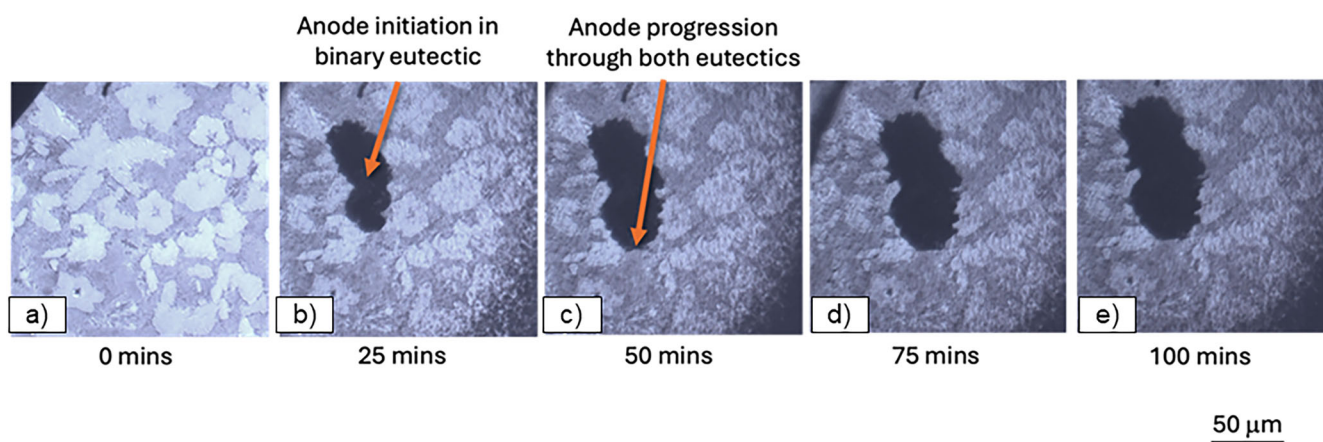
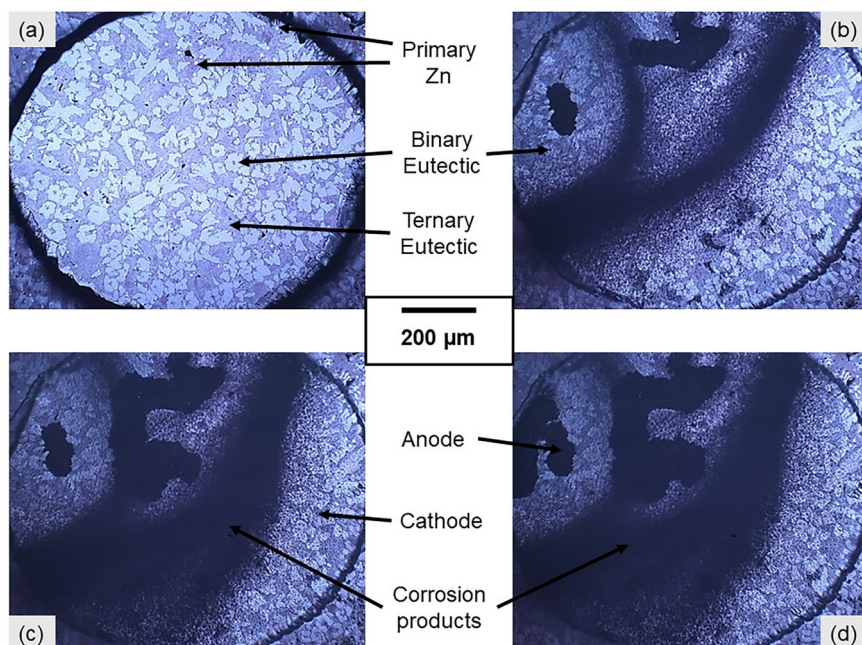
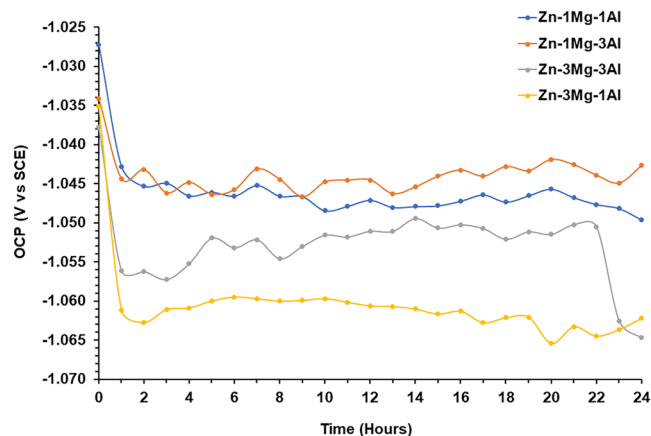


**Fig. 11 | Time-lapse Microscopy images of Zn-3Mg-3Al taken under immersion conditions in 0.17 mol.L<sup>-1</sup> NaCl pH 7 solution. The images taken at (a) 0 min (b) 25 min (c) 50 min (d) 75 min and e 100 min show the initiation and progression of an anode over the first 100 min of exposure.**

**Table 4 | Area fraction of phases present in ZMA samples exposed to electrolyte during TLM experiments**

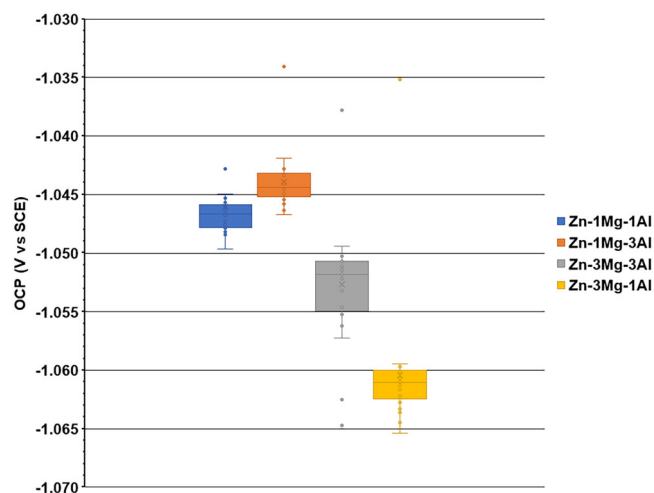
Sample	Primary Zn (%)	Eutectic (%)
Zn-1Mg-1Al	57.59	42.41
Zn-1Mg-3Al	23.78	76.22
Zn-3Mg-1Al	11.19	88.81
Zn-3Mg-3Al	0.31	99.69

Figure 17 shows the normal current density measured above the freely corroding surface of ZMA coatings in pH 7 0.17 mol.L<sup>-1</sup> NaCl for 1, 6, 12, 18 and 24 h. Peak anodic current densities of ~15 A.m<sup>-2</sup> are recorded. In all four coatings, anodic (red) activities and cathodic (blue) activities were detected from the first hour (1 h). For the base coating Zn-1Mg-1Al, the number of localised anodes and the intensity of anodic as well as cathodic activities are much greater compared to the other three modified coatings. In



**Fig. 12 | The time-dependent OCP for all four ZMA coatings immersed in 0.17 mol.L<sup>-1</sup> NaCl pH 7 solution for 24 h. All coatings exhibited relatively stable potentials after ~2 h of exposure.**





**Fig. 13** | Box plots summarising all repeated OCP measurements made over 24 h in 0.17 mol.L<sup>-1</sup> NaCl pH 7 for ZMA coatings. The image summarises the effect of Mg and Al additions to the OCP of coatings with respect to the base Zn-Mg-Al.

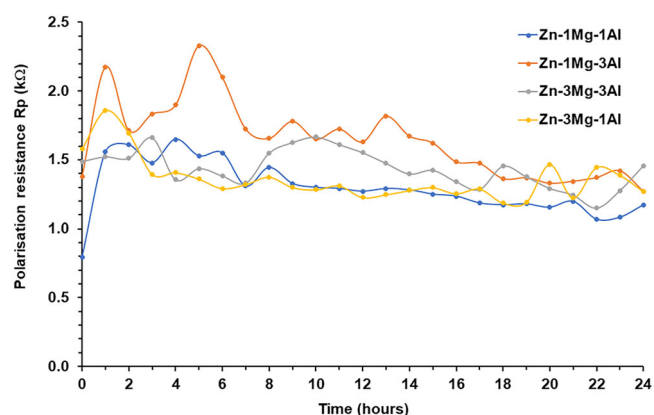


**Fig. 14** | LPR measured over 24 h in 0.17 mol.L<sup>-1</sup> NaCl pH 7 solution for ZMA coatings. The image shows the rate of corrosion for all four coatings with respect to time.

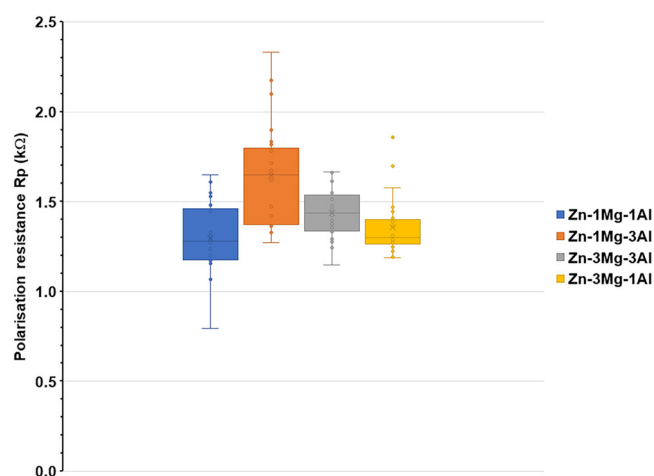


**Fig. 15** | Box plots summarising all repeated LPR measurements made over 24 h in 0.17 mol.L<sup>-1</sup> NaCl pH 7 for ZMA coatings. The image summarises the effect of Mg and Al additions on the median corrosion rate of coatings with respect to the base Zn-Mg-Al.

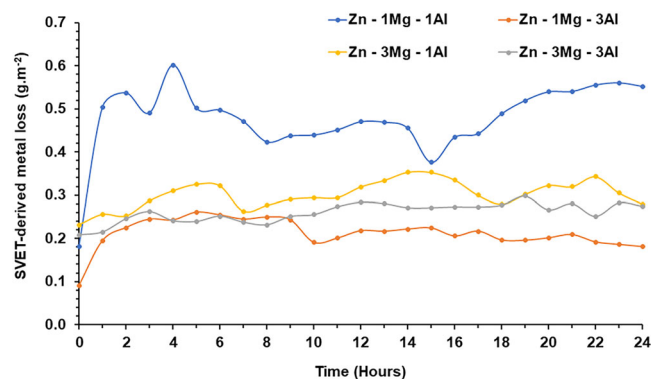


**Fig. 16** | SVET-derived metal loss for ZMA coatings. The average hourly metal loss as a function of time for ZMA coatings after immersion in 0.17 mol.L<sup>-1</sup> NaCl pH 7 for 24 h.

**Table 5** | SVET-derived metal loss for ZMA samples after immersion in 1 wt. % NaCl pH 7 for 24 h

Sample	Average (g.m <sup>-2</sup> )
Zn-1Mg-1Al	11.48 ± 0.12
Zn-1Mg-3Al	5.31 ± 0.07
Zn-3Mg-1Al	7.54 ± 0.06
Zn-3Mg-3Al	6.49 ± 0.07

addition, the anode (I marked on 1 h SVET map, Fig. 17) established at 1 h was still active at 24 h however, there was a slight decrease in its intensity. In contrast, for the other three modified coatings, the individual anodes established at 1 h (II–IV marked on 1 h SVET map, Fig. 17) have deactivated/passivated by 24 h.

## Discussion

In the base coating, Zn-1Mg-1Al, initiation and progression of corrosion occurred in the interdendritic eutectic regions. SEM/EDX analysis reported here and in our previous work has shown this is mainly binary eutectic composed of Zn and IMs of Mg & Zn, predominantly MgZn<sub>2</sub><sup>17</sup>. The initiation of corrosion occurs in the eutectic due to galvanic effects of IMs such as MgZn<sub>2</sub>, Mg<sub>2</sub>Zn<sub>11</sub> and Mg<sub>2</sub>Zn<sub>3</sub> with respect to Zn. It has previously been reported that the IM MgZn<sub>2</sub> has a low free corrosion potential of -1.4 V vs saturated calomel electrode (SCE)<sup>33,34</sup> with Mg<sub>2</sub>Zn<sub>11</sub> and Mg<sub>2</sub>Zn<sub>3</sub> also displaying similar potentials to MgZn<sub>2</sub><sup>35</sup>. These IMs are the most thermodynamically and kinetically active phase in the coating, as demonstrated by this preferential initiation and subsequent preferential progression of anodic attack through the eutectic regions. At neutral pH corrosion of the IMs can release both Mg<sup>2+</sup> and Zn<sup>2+</sup> congruently into the electrolyte at the anode<sup>34</sup>. The Zn dendrites often remain as intact islands due to these local galvanic differences in potential, with the Zn having a more noble free corrosion potential<sup>14</sup>. Zn dendrites will thus tend to act as preferential sites for cathodic oxygen reduction ( $O_2 + 2H_2O + 4e^- \rightarrow 4OH^-$ ) due to these galvanic effects and the relative decrease of cathodic kinetics associated with the eutectic phases due to the presence of MgO/Mg(OH)<sub>2</sub> and Al<sub>2</sub>O<sub>3</sub>/Al(OH)<sub>3</sub> at their surfaces that are both wide-band semi-conductors/insulators in contrast to the semi-conducting nature of ZnO/Zn(OH)<sub>2</sub><sup>34</sup>. Additionally, the Zn regions of the eutectic phases are inferior cathodes kinetically than the Zn dendrites due to the lamellar nature of their microstructures, which create a discontinuous surface for cathodic activity. After some time, the Zn dendrites also become susceptible to anodic attack once the regions of eutectic surrounding the dendrites are corroded away and local galvanic effects are diminished.

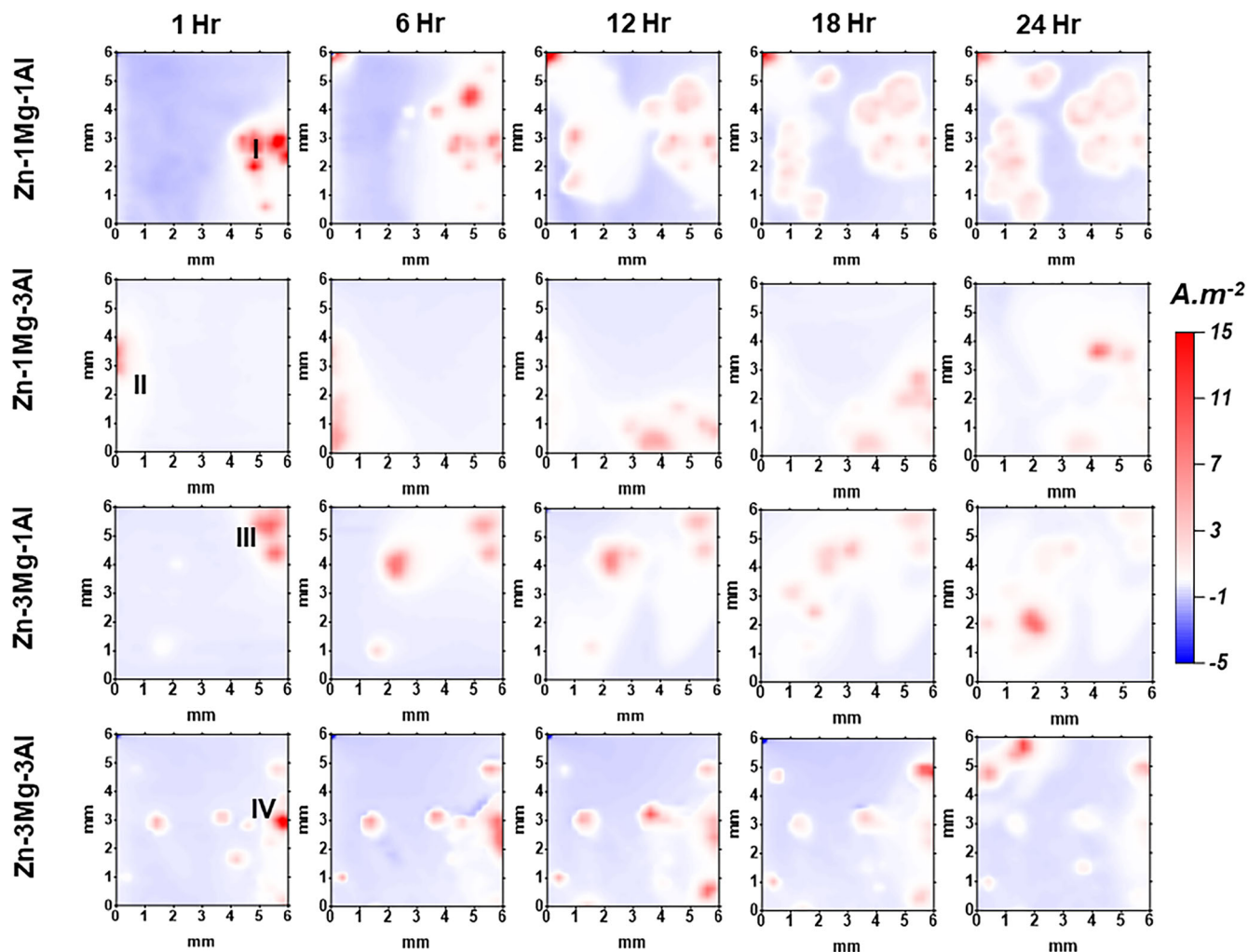
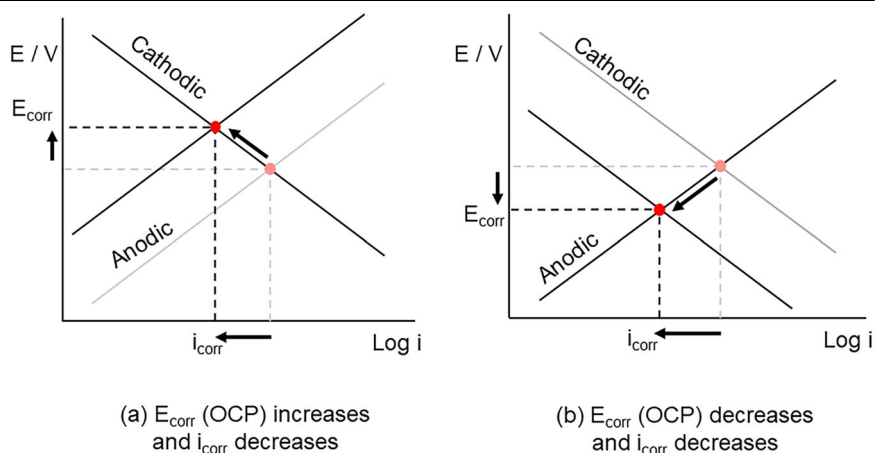


**Fig. 17 | SVET colour maps representing normal current density measured above ZMA surfaces immersed in 0.17 mol.L<sup>-1</sup> pH 7 solution for 24 h. The maps presented are of 1, 6, 12, 18 and 24 h of immersion time for Zn-1Mg-1Al, Zn-1Mg-3Al,**

**Zn-3Mg-1Al and Zn-3Mg-3Al. Anodic activities are shown in red and cathodic activities are shown in blue.**

**Fig. 18 | Evans diagrams demonstrating the difference in corrosion deactivation mechanism.**

**a** Shows the anodic deactivation and **b** shows the cathodic deactivation mechanism. The figure provides a visual explanation of the anodic and cathodic deactivation of the corrosion mechanism in Zn-Mg-Al.



When the Al level was increased to 3 wt.%, a significant change in the corrosion behaviour was observed whereby the OCP of the coating (Zn-1Mg-3Al) was increased and the corrosion kinetics ( $i_{\text{corr}}$ ) decreased over 24 hours. This phenomenon is schematically presented in Fig. 18a and can be seen that such changes in OCP and  $i_{\text{corr}}$  may occur through modifications

to the anodic reaction, leading to anodic deactivation of the coating. This change in anodic behaviour can be explained with regards to changes in the microstructure of the coating where the volume fraction, and critically, the surface area fraction of the eutectic phase increased by 14 and 34% respectively. In addition, this eutectic was mainly Al-containing ternary



eutectic rather than binary eutectic. Furthermore, an additional Al-rich dendritic phase was present in the microstructure that did not occur in the base alloy. In the Zn-1Mg-3Al coating, anode progression occurred through primary Zn dendrites in addition to areas of eutectic in contrast to the preferential eutectic attack observed in the base Zn-1Mg-1Al coating. The Al-rich phases remained uncorroded during the exposure time of the experiment.

The presence of a greater surface area fraction of ternary eutectic and the Al-rich dendritic phase leads to a greater surface coverage of  $\text{Al}_2\text{O}_3/\text{Al}(\text{OH})_3$ , which improves the surface passivity<sup>36</sup> at the initial experimental pH of 7. This passive layer tends to reduce the thermodynamic likelihood of oxidation, hence the rise in OCP of this alloy. Although the eutectic phase was often the site of anodic initiation due to the presence of Zn/Mg IMs, the overall activity of the eutectic is reduced due to the passive  $\text{Al}_2\text{O}_3/\text{Al}(\text{OH})_3$  associated with the Al component of the eutectic. Therefore, the emphasis of anodic activity on the IMs is reduced, enabling the primary Zn dendrites to become focal anodic sites. Zn is a less kinetically active phase compared to IMs that were preferentially attacked in the base coating, and hence the alloy is anodically deactivated. The reduction in surface area fraction of primary Zn can also lead to a reduction in cathodic activity as the Zn dendrites will be the most likely sites of cathodic activity due to the poor electrocatalytic kinetics of  $\text{Al}_2\text{O}_3/\text{Al}(\text{OH})_3$ . The net effect, however, is that of anodic deactivation due to a greater degree of surface passivation and the focal anodic dissolution now being that of Zn.

Increasing the Mg levels to 3 wt. % (Zn-3Mg-1Al) also influenced the corrosion behaviour of the coating with a decrease in the OCP and a decrease in the corrosion rate ( $i_{\text{corr}}$ ). This phenomenon is schematically presented in Fig. 18b and can be seen that such changes in OCP and kinetics may occur through a change in the cathodic reaction leading to cathodic deactivation of the coating. The increase in Mg led to a 46% increase in both the volume fraction and the surface area fraction of the eutectic phases. This surface area fraction was dominated by a binary eutectic with small regions of ternary (Al-containing) phases. For Zn-3Mg-1Al, anodes preferentially initiated and propagated through the binary eutectic due to the presence of the most active phase in terms of thermodynamics and kinetics,  $\text{MgZn}_2$ , and other IMs ( $\text{Mg}_2\text{Zn}_{11}$  and  $\text{Mg}_7\text{Zn}_3$ ), similar to the behaviour of base Zn-1Mg-1Al. The observed cathodic deactivation can be explained by the surface area fraction of the phases present. In Zn-3Mg-1Al, as anodic activity is concentrated at eutectic phases the cathodic oxygen reduction will tend to occur on the primary Zn dendrites due to galvanic and kinetic effects. The binary and ternary eutectic phases are not as efficient cathodes for oxygen reduction due to the presence of insulating  $\text{MgO}/\text{Mg}(\text{OH})_2$  and  $\text{Al}_2\text{O}_3/\text{Al}(\text{OH})_3$ . In this coating, the area fraction of eutectic increased and primary Zn was reduced compared to the base coating Zn-1Mg-1Al, subsequently reducing the galvanic driving force between the primary Zn and the eutectic phase. Additionally, the release of  $\text{Mg}^{2+}$  into the solution and the formation of Mg hydroxide have been shown to buffer the  $\text{pH} \geq 9$ , promoting the formation of a more insulating LDH that reduces the corrosion kinetics<sup>10,19</sup>. Hence, the combination of the reduced area of Zn, an increased surface area of less cathodically active phases, and the formation of stable corrosion products leads to an overall cathodic deactivation of the alloy.

Increasing both the Mg & Al levels to 3 wt. % (Zn-3Mg-3Al) led to a complete change in the coating microstructure with the formation of an almost wholly eutectic microstructure (99.69%). The eutectic was a mixture of binary and ternary, with anodes preferentially initiating in the binary phase. This occurred because the binary eutectic is not protected by a passive  $\text{Al}_2\text{O}_3/\text{Al}(\text{OH})_3$  layer due to the absence of Al, whereas the ternary eutectic will have such protection. As such, initial anode initiation and progression through the binary eutectic is more favourable.

Increasing the Mg and Al levels to 3 wt. % caused a decrease in the OCP and a decrease in the corrosion rate ( $i_{\text{corr}}$ ) with respect to the base Zn-1Mg-1Al, indicative of cathodic deactivation as shown in Fig. 18(b). As the microstructure of Zn-3Mg-3Al is almost wholly eutectic, the efficiency of cathodic oxygen reduction will be reduced compared to the base coating due to the presence of  $\text{MgO}/\text{Mg}(\text{OH})_2$  and  $\text{Al}_2\text{O}_3/\text{Al}(\text{OH})_3$  over most of the surface.

Thus, the kinetics associated with oxygen reduction are less efficient in comparison to the base coating and the system becomes cathodically deactivated.

Figure 19 (a–d) shows schematically a summation of the effects of varying Al and Mg levels with respect to microstructures, surface oxides in terms of their relative cathodic electrocatalytic kinetics, likely preferential sites of anodic and cathodic activity and the overall net impact on corrosion in comparison to the base Zn-1Mg-1Al alloy.

Figure 20 summarises the effect of alloy addition with respect to the mix-potential and kinetics of corrosion. Anodic deactivation through increased Al additions provided the largest reduction in corrosion kinetics of 16–17%. Mg additions alone provided a small decrease in corrosion kinetics of approximately 3% whilst the combination of both additions reduced the corrosion rate by around 7% with both alloys showing cathodic deactivation. It is interesting why the sample with 3 wt.% Mg and 3 wt.% Al had a lower performance than the alloy with the Al level alone raised to 3 wt.%. A possible explanation for this is that the release of  $\text{Mg}^{2+}$  ions from preferential attack of the binary eutectic enables the pH of the interfacial electrolyte to rise and cause dissolution of the  $\text{Al}_2\text{O}_3/\text{Al}(\text{OH})_3$  associated with the ternary eutectic thereby reducing the passive effects of these products. Ternary eutectic attack was observed in Figs. 10 and 11 but only after initial corrosion of the binary eutectic supporting this postulation.

Considering both Figs. 19 and 20 it was shown that the surface microstructure engendered through Mg and Al additions is critical in determining the subsequent mechanisms and extent of corrosion. These data have shown that in terms of initial corrosion mechanisms, the addition of Al has the largest effect on corrosion behaviour and as such, to maximise surface corrosion performance the formation of ternary eutectic and Al-rich phases with reduced levels of Zn dendrites at the surface should be prioritised through alloying additions and production conditions.

In conclusion, a systematic study into the effects of Al and Mg variations on the microstructure and its subsequent corrosion behaviour afforded by HDG ZMA coatings has been completed to show that;

- Preferential eutectic corrosion was observed in the base Zn-1Mg-1Al coating due to the galvanic activity of Zn/Mg IMs in the eutectic phases.
- Increasing the Al and Mg to 3 wt. % independently increased the formation of the eutectic phases (both volume fraction and surface area fraction) and reduced the primary Zn. However, for Zn-1Mg-3Al the formed eutectic phase was wholly ternary eutectic with additional Al-rich phases in the microstructure whereas for Zn-3Mg-1Al the formed eutectic phase was mainly binary eutectic with small patches of ternary eutectic.
- Increasing Al and Mg simultaneously to 3 wt. % also increased the formation of the eutectic phases with an area surface fraction of 99% and volume fraction of 94%.
- Improved corrosion performance through an anodic deactivation mechanism was observed when surface levels of ternary eutectic and Al-rich phases were present through Al additions to 3 wt.% (Zn-1Mg-3Al). The highest improvement in corrosion performance was also observed for this alloy.
- Mg additions to 3 wt.% (Zn-3Al-1Mg) also demonstrated improved corrosion performance due to cathodic deactivation of the coating however the reduction in corrosion rate was not as great as for increased Al additions (Zn-1Mg-3Al).
- Increasing both Al and Mg to 3 wt.% (Zn-3Mg-3Al) demonstrated an overall cathodic deactivation of the system and gave improved performance over the base coating Zn-1Mg-1Al.
- Alloying additions can be controlled to maximise the formation of Al-containing phases at a ZMA coating's surface to reduce its corrosion rate.

## Methods

### Materials

The Surtex A5 HDPS housed at Swansea University's Coating and Corrosion group was used to produce ZMA coatings on steel substrates. A 0.7 mm gauge cold-rolled DX-51 steel with dimensions of 220 × 110 mm was used as the base substrate. Steel substrates were cleaned with a surfactant,

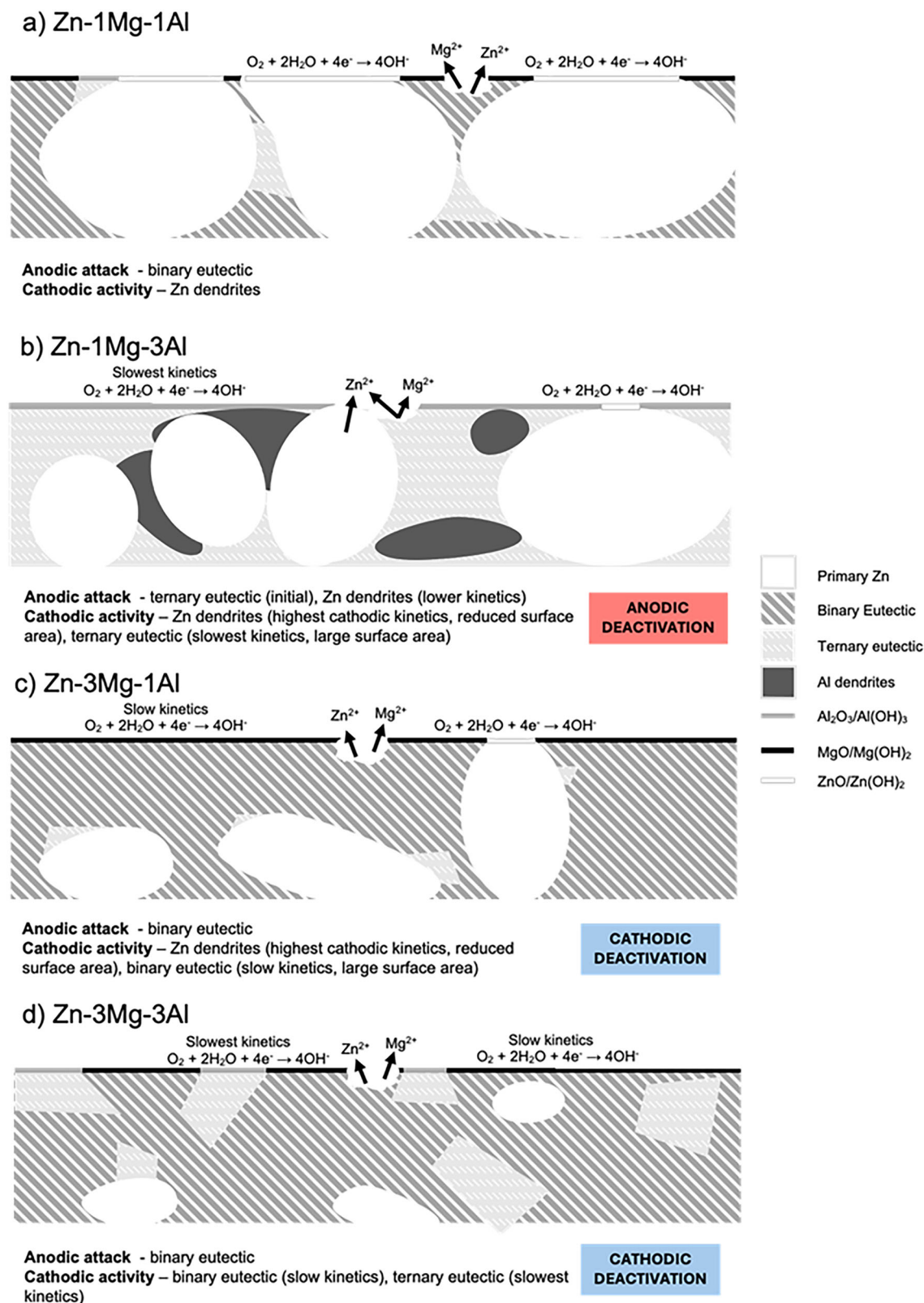


**Fig. 19 | Summary of corrosion mechanisms.** The images show the schematic representation of changes to microstructure and subsequent effects on corrosion mechanisms for **a** Zn-1Mg-1Al **b** Zn-1Mg-3Al **c** Zn-3Mg-1Al **d** Zn-3Mg-3Al.

followed by an acetone rub to remove oil and surface contamination. The atmosphere was 7% H<sub>2</sub> remainder N<sub>2</sub> with a dew point of −40 °C. The annealing cycle used for the ZMA coatings production is presented in Fig. 21. Post-production, samples were stored in a desiccator to prevent atmospheric corrosion. The ZMA coatings were ~25 μm thick (~250 g.m<sup>−2</sup>).

Chemicals; sodium hydroxide (NaOH), ethanol (C<sub>2</sub>H<sub>5</sub>OH), nitric acid (HNO<sub>3</sub>) and hydrochloric acid (HCl) used during the investigation were of analytical grade purity and purchased from Sigma-Aldrich Chemical Co. A 0.17 mol.L<sup>−1</sup> NaCl pH 7 solution was used throughout, and the pH of the bulk solution was adjusted using



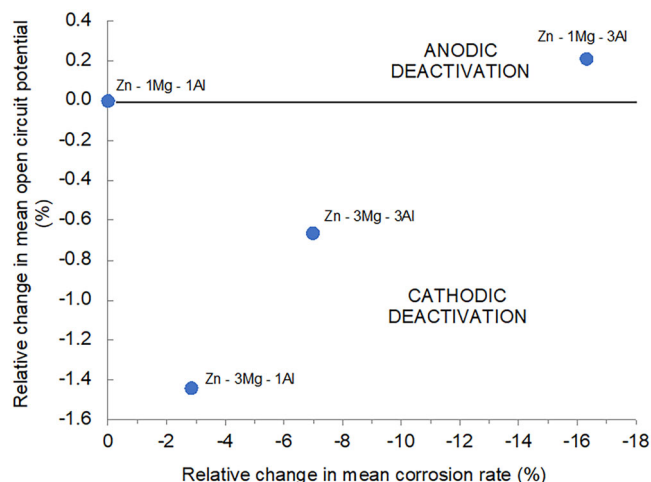


**Fig. 20 | Summary of the mixed-potential and kinetics of ZMA coatings.** The image shows the effects of Mg and Al additions on the OCP and the corrosion rate of ZMA coatings.

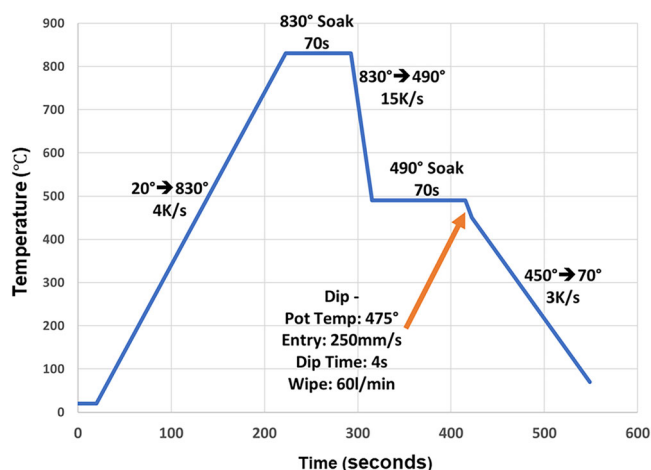


**Fig. 21 | Annealing cycle used during the production of ZMA coatings.** The image shows the heating and cooling rate used during the production of the ZMA experimental samples.

aqueous NaOH or HCl. All the corrosion experiments were conducted at room temperature.

### Microstructure analysis

In all cases, 2 × 2 cm steel coupons coated with ZMA coatings were hot-mounted in non-conductive phenolic resin (Metprep Limited). The samples were then polished with aqueous 1 μm diamond suspensions and rinsed with distilled water, followed by ethanol. The polished samples were etched using 3 wt. % Nital to reveal the microstructure. A Hitachi TM3000 Scanning Electron Microscope (SEM) with Bruker EDS module was employed to capture microstructural images and conduct EDS analysis. Carbon tape was used to obtain electrical connections during SEM imaging. SEM cross-section images were analysed using Adobe Photoshop software (APS) to determine the volume fraction of different microstructural phases. The APS was calibrated by setting a number of pixels to an already-known length, the scale bar, within the SEM image. A Bruker D8 Discover X-ray Diffractometer (XRD) with a copper point source (40 kV and 40 mA) was utilised to identify the different phases within the coatings. XRD scans were conducted in true parallel beam mode using a Goebel mirror, equatorial soller, 1 mm collimator and 0.6 mm slit.

Inductively coupled plasma (ICP)-optical emission spectroscopy (OES); The coating was removed from a circular area with a radius of 6 cm using HCl as per EN 10346 (Annex A)<sup>37</sup>. The solution containing the removed coating was transferred to a volumetric flask and a ICP-OES spectrometer Spectroblue SOP FMX 26 (Spectro Analytical Instruments) was utilised to examine coating composition.

### Time-lapse microscopy (TLM)

TLM consists of a Meiji Techno 7100 optical microscope fitted with an Infinity 2 digital camera. A polyethene shroud with an integrated glass window was placed over the microscope lens, enabling the acquisition of microstructural images of corroding surfaces under immersion conditions. The detailed methodology of TLM has been described elsewhere<sup>17,18</sup>. Previously, TLM has been used to understand the corrosion mechanism of Zn-based coating alloys<sup>14,17,18,23,38</sup>. The samples were prepared as mentioned in section 4.2. A circular area with a diameter of 1 mm was masked off using polytetrafluoroethylene (PTFE) tape and was exposed to the electrolyte. An image was taken every two minutes, and the still images were compiled into time-lapse videos using Microsoft Movie Maker software.

### Electrochemical measurements

All electrochemical (and TLM imaging) experiments were carried out at or close to (±15 mV) OCP. The development of pH gradients across a surface containing both anodes and cathodes has been shown to be important in determining the corrosion mechanisms of these alloys. A recent study by Han et al. has shown that potentiodynamic polarisation sweeps under conditions of mild alkalinity can drastically alter the predominant corrosion species from the surface of these alloys, measured directly using ICP-AE,S leading to underpredictions of true corrosion rates<sup>39</sup>. The disruption of surface pH gradients induced through potentiodynamic sweeps beyond ±15 mV has therefore been avoided to more closely assess the open circuit behaviour of these alloys.

A Gamry Interface 1010E potentiostat was used to perform the OCP and LPR measurements using a 3-electrode set-up. An SCE and platinum electrode were used as the reference electrode and the counter electrode, respectively. An area of 0.78 cm<sup>2</sup> was exposed to the electrolyte. The measurements were initiated as soon as the electrolyte was introduced and were recorded hourly for a period of 24 h. OCP measurements were recorded for 300 s at the start of each hour followed by a LPR measurement using a polarisation of ±15 mV relative to the measured OCP. The short duration of the LPR measurement ensured that the alloy was corroding under open circuit condition for the majority of each hour. Three repeat experiments were performed for each alloy composition.

### Scanning vibrating electrode technique (SVET)

The SVET experimental setup and calibration process have been described in previous literature<sup>40–43</sup>. In brief, SVET consists of a 125 μm diameter glass-encased platinum wire microtip vibrating perpendicularly at a constant frequency of 140 Hz with an amplitude of 25 μm at a height of 100 μm from the corroding surface. The SVET detects the alternating potential at which the probe vibrates, enabling monitoring of the temporal and spatial corrosion behaviour of the material. In addition, SVET also enables the calculation of metal loss; however, it is considered semi-quantitative since multiple assumptions are made. It is assumed that Zn<sup>2+</sup> (Zn ions) are released during the anodic activities and remain constant between the scans. The SVET metal loss calculation procedure is discussed in detail elsewhere, along with the SVET limitations<sup>14,23,38,44</sup>. The samples were rinsed using deionised water and ethanol. An area of 36 mm<sup>2</sup> masked off using 3 M PTFE tape was exposed to the electrolyte. Thirty-one measurements were made along both the length and width of the exposed area. Measurements were taken at an interval of 1 over 24 h period. Three repeats were conducted for each sample.

### Data availability

The raw/processed data required to reproduce these findings cannot be shared at this time as the data also forms part of an ongoing study.

Received: 20 May 2025; Accepted: 16 July 2025;

Published online: 29 July 2025

## References

- Kainuma, S. et al. Corrosion protection of steel members using an Al-Zn base sacrificial anode and fiber sheet in an atmospheric environment. *Constr. Build. Mater.* **224**, 880–893 (2019).
- Ding, C. et al. Research on design and microstructure of hot-dip Zn-Al-Mg/Sn alloy. *Mater. Charact.* **185**, 111746 (2022).
- Farahany, S. et al. Microstructure development, phase reaction characteristics and properties of quaternary Zn-0.5Al-0.5Mg-xBi hot dipped coating alloy under slow and fast cooling rates. *Surf. Coat. Technol.* **315**, 112–122 (2017).
- Prosek, T., Persson, D., Stoullil, J. & Thierry, D. Composition of corrosion products formed on Zn-Mg, Zn-Al and Zn-Al-Mg coatings in model atmospheric conditions. *Corros. Sci.* **86**, 231–238 (2014).
- Lee, J.-W. et al. Mechanistic study on the cut-edge corrosion behaviors of Zn-Al-Mg alloy coated steel sheets in chloride containing environments. *Corros. Sci.* **160**, 108170 (2019).
- Volovitch, P. et al. Understanding corrosion via corrosion product characterization: II. Role of alloying elements in improving the corrosion resistance of Zn-Al-Mg coatings on steel. *Corros. Sci.* **53**, 2437–2445 (2011).
- Salgueiro Azevedo, M., Allély, C., Ogle, K. & Volovitch, P. Corrosion mechanisms of Zn(Mg, Al) coated steel in accelerated tests and natural exposure: 1. The role of electrolyte composition in the nature of corrosion products and relative corrosion rate. *Corros. Sci.* **90**, 472–481 (2015).
- Elvins, J., Spittle, J. A., Sullivan, J. H. & Worsley, D. A. The effect of magnesium additions on the microstructure and cut edge corrosion resistance of zinc aluminium alloy galvanised steel. *Corros. Sci.* **50**, 1650–1658 (2008).
- Duchoslav, J. et al. Evolution of the surface chemistry of hot dip galvanized Zn-Mg-Al and Zn coatings on steel during short term exposure to sodium chloride containing environments. *Corros. Sci.* **91**, 311–320 (2015).
- Prosek, T. et al. Corrosion mechanism of model zinc-magnesium alloys in atmospheric conditions. *Corros. Sci.* **50**, 2216–2231 (2008).
- Yao, C. et al. Effect of Mg content on microstructure and corrosion behavior of hot dipped Zn-Al-Mg coatings. *J. Alloy. Compd.* **670**, 239–248 (2016).
- Wint, N. et al. The kinetics and mechanism of filiform corrosion occurring on zinc-aluminium-magnesium coated steel. *Corros. Sci.* **158**, 108073 (2019).
- Prosek, T. et al. Improving corrosion stability of Zn[ $\text{Sn}$ ]/Al[ $\text{Sn}$ ]/Mg by alloying for protection of car bodies. *Surf. Coat. Technol.* **306**, 437–439 (2016).
- Wint, N. et al. The ability of Mg<math>2\text{Ge}</math> crystals to behave as ‘smart release’ inhibitors of the aqueous corrosion of Zn-Al-Mg alloys. *Corros. Sci.* **179**, 109091 (2021).
- Prosek, T., Persson, D., Stoullil, J. & Thierry, D. Composition of corrosion products formed on Zn-Mg, Zn-Al and Zn-Al-Mg coatings in model atmospheric conditions. *Corros. Sci.* **86**, 231–238 (2014).
- Prosek, T. et al. Effect of the microstructure of Zn-Al and Zn-Al-Mg model alloys on corrosion stability. *Corros. Sci.* **110**, 71–81 (2016).
- Sullivan, J. et al. In situ monitoring of corrosion mechanisms and phosphate inhibitor surface deposition during corrosion of zinc-magnesium-aluminium (ZMA) alloys using novel time-lapse microscopy. *Faraday* **180**, 361–379 (2015).
- Sullivan, J., Mehraban, S. & Elvins, J. In situ monitoring of the microstructural corrosion mechanisms of zinc-magnesium-aluminium alloys using time lapse microscopy. *Corros. Sci.* **53**, 2208–2215 (2011).
- Schuerz, S. et al. Corrosion behaviour of Zn-Al-Mg coated steel sheet in sodium chloride-containing environment. *Corros. Sci.* **51**, 2355–2363 (2009).
- Hausbrand, R., Stratmann, M. & Rohwerder, M. Corrosion of zinc-magnesium coatings: mechanism of paint delamination. *Corros. Sci.* **51**, 2107–2114 (2009).
- Volovitch, P., Allely, C. & Ogle, K. Understanding corrosion via corrosion product characterization: I. Case study of the role of Mg alloying in Zn-Mg coating on steel. *Corros. Sci.* **51**, 1251–1262 (2009).
- Salgueiro Azevedo, M., Allély, C., Ogle, K. & Volovitch, P. Corrosion mechanisms of Zn(Mg,Al) coated steel: 2. The effect of Mg and Al alloying on the formation and properties of corrosion products in different electrolytes. *Corros. Sci.* **90**, 482–490 (2015).
- Wint, N. et al. The effect of microstructural refinement on the localized corrosion of model zn-al-mg alloy coatings on steel. *J. Electrochem. Soc.* **166**, C3147–C3158 (2019).
- Persson, D., Thierry, D., LeBozec, N. & Prosek, T. In situ infrared reflection spectroscopy studies of the initial atmospheric corrosion of Zn-Al-Mg coated steel. *Corros. Sci.* **72**, 54–63 (2013).
- Duchoslav, J. et al. Structure and chemistry of surface oxides on ZnMgAl corrosion protection coatings with varying alloy composition. *Surf. Coat. Technol.* **368**, 58 (2019).
- Malla, A. D. et al. Mechanistic investigation on the influence of coating weights on the corrosion behaviour of hot-dip-galvanised Zn-Mg-Al coatings. *npj Mater. Degrad.* **8**, 78 (2024).
- Rai, P. K. et al. Corrosion behaviour of hot-dip Zn-Al-Mg coatings with different Al content. *Anti-Corros. Methods Mater.* **69**, 29–37 (2022).
- Ma, Z. et al. Effect of Al and Sn on the microstructure, micro-hardness and corrosion properties of Zn-Al-Mg coatings. *Mater. Today Commun.* **33**, 104892 (2022).
- Rai, P. K. et al. Effect of magnesium on corrosion behavior of hot-dip Zn-Al-Mg coating. *J. Mater. Eng. Perform.* **30**, 4138–4147 (2021).
- Han, D. et al. Study on the microstructure and corrosion resistance of Zn-3Al-xMg alloy. *Surf. Coat. Technol.* **473**, 130011 (2023).
- Zhang, Z. et al. Effect of Al/Mg ratio on the microstructure and phase distribution of Zn-Al-Mg coatings. *Metals* **13**, 1963 (2023).
- Zhang, Z. et al. Effects of Al-Mg on the microstructure and phase distribution of Zn-Al-Mg coatings. *Metals* **13**, 46 (2022).
- Ikeuba, A. I. et al. Understanding the electrochemical behavior of bulk-synthesized MgZn 2 intermetallic compound in aqueous NaCl solutions as a function of pH. *J. Solid State Electrochem.* **23**, 1165–1177 (2019).
- Han, J. & Ogle, K. Editors’ choice—dealloying of MgZn 2 intermetallic in slightly alkaline chloride electrolyte and its significance in corrosion resistance. *J. Electrochem. Soc.* **164**, C952–C961 (2017).
- Byun, J. M. et al. Corrosion behavior of Mg<sub>2</sub>Zn<sub>11</sub> and MgZn<sub>2</sub> single phases. *Korean J. Met. Mater.* **51**, 413–419 (2013).
- Sullivan, J., Penney, D., Elvins, J. & Khan, K. The effect of ultrasonic irradiation on the microstructure and corrosion rate of a Zn–4.8 wt. % Al galvanising alloy used in high performance construction coatings. *Surf. Coat. Technol.* **306**, 480–489 (2016).
- British Standards Institution. CEN. EN 10346: Continuously hot-dip coated steel flat products for cold forming. Technical delivery conditions. (Available at: <https://knowledge.bsigroup.com/products/continuously-hot-dip-coated-steel-flat-products-for-cold-forming-technical-delivery-conditions>) (Accessed: 4 May 2025). (2015).
- Malla, A. D. et al. Mechanistic study on the corrosion behaviour of Zinc and Zinc-Calcium alloys designed for enhanced metallic coatings in the presence of chloride and phosphate ions. *Corros. Sci.* **213**, 110956 (2023).
- Han, J. & Ogle, K. Element-resolved electrochemical database: AESEC polarization curves of ZnAlMg alloy coating constituents, 28 April 2025, PREPRINT (Version 1) available at Research Square, <https://doi.org/10.21203/rs.3.rs-6511055/v1> (2025).
- Williams, G. & Neil McMurray, H. Localized corrosion of magnesium in chloride-containing electrolyte studied by a scanning vibrating electrode technique. *J. Electrochem. Soc.* **155**, C340 (2008).



41. Williams, G., McMurray, H. N. & Grace, R. Inhibition of magnesium localised corrosion in chloride containing electrolyte. *Electrochim. Acta* **55**, 7824–7833 (2010).
42. Böhm, S., McMurray, H. N., Powell, S. M. & Worsley, D. A. Photoelectrochemical investigation of corrosion using scanning electrochemical techniques. *Electrochim. Acta* **45**, 2165–2174 (2000).
43. Bastos, A. C., Quevedo, M. C., Karavai, O. V. & Ferreira, M. G. S. Review—on the application of the scanning vibrating electrode technique (SVET) to corrosion research. *J. Electrochem. Soc.* **164**, C973 (2017).
44. Sheikholeslami, S. et al. Cut-edge corrosion behavior assessment of newly developed environmental-friendly coating systems using the scanning vibrating electrode technique (SVET). *Corros. Sci.* **192**, 109813 (2021).

## Acknowledgements

The authors would like to thank the Galvanised Autobody Partnership programme for funding and its associated members for their valuable input.

## Author contributions

A.D.M: Investigation, methodology, data curation, formal analysis, writing—original draft, writing—review & editing, validation. J.H.S: Conceptualisation, methodology, validation, formal analysis, supervision, writing—original draft, writing—review & editing, funding acquisition, resources. D.J.P: Conceptualisation, methodology, validation, formal analysis, supervision, writing—original draft, writing—review & editing, funding acquisition, resources. D.A.B: Investigation, data curation. G.W: Writing—review & editing, validation, supervision, resources. F.E.G: Writing—review, resources. A.P. D.C: Writing—review, resources. T.R: Investigation, data curation.

## Competing interests

The authors declare no competing interests.

## Additional information

**Supplementary information** The online version contains supplementary material available at <https://doi.org/10.1038/s41529-025-00647-x>.

**Correspondence** and requests for materials should be addressed to A. D. Malla.

**Reprints and permissions information** is available at <http://www.nature.com/reprints>

**Publisher's note** Springer Nature remains neutral with regard to jurisdictional claims in published maps and institutional affiliations.

**Open Access** This article is licensed under a Creative Commons Attribution 4.0 International License, which permits use, sharing, adaptation, distribution and reproduction in any medium or format, as long as you give appropriate credit to the original author(s) and the source, provide a link to the Creative Commons licence, and indicate if changes were made. The images or other third party material in this article are included in the article's Creative Commons licence, unless indicated otherwise in a credit line to the material. If material is not included in the article's Creative Commons licence and your intended use is not permitted by statutory regulation or exceeds the permitted use, you will need to obtain permission directly from the copyright holder. To view a copy of this licence, visit <http://creativecommons.org/licenses/by/4.0/>.

© The Author(s) 2025